Nanoscale

Accepted Manuscript

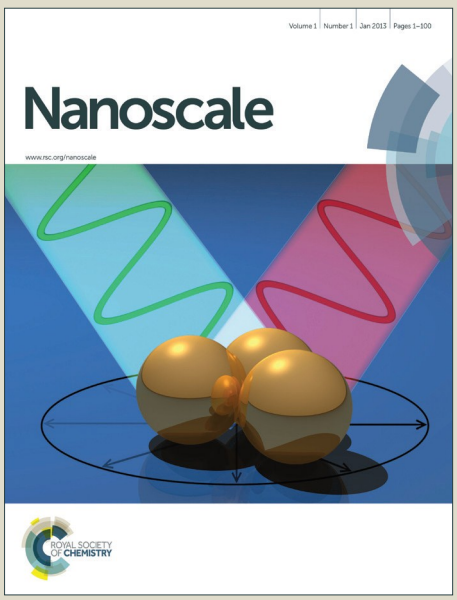

ROYAL SOCIETY OF CHEMISTRY

www.rsc.org/nanoscale

Bone-repair properties of biodegradable hydroxyapatite nano-rods superstructures

Noelia L. D' Elía[(a)], Colleen Mathieu[(b)], Caroline D. Hoemann[(b, c, d)], Juan A. Laiuppa[(e)], Graciela E. Santillan[(e)], Paula V. Messina*[(a)].

(a) Department of Chemistry, Universidad Nacional del Sur, (8000) Bahía Blanca, Argentina. INQUISUR-CONICET. (b) Institute of Biomedical Engineering, École Polytechnique, Montréal, QC, Canada. (c) Groupe de Recherche en Sciences et Technologies Biomédicales (GRSTB), Canada. (d) Department of Chemical Engineering, École Polytechnique, Montréal, QC, Canada. (e) Department of Biology, Biochemistry and Pharmacy, Universidad Nacional del Sur, (8000) Bahía Blanca, Argentina.

* Author to whom correspondence should be addressed. Tel: +54 291 4595159. Fax: +54 291 4595160. Electronic mail: pmessina@uns.edu.ar.

Abstract: Nano-hydroxyapatite (nano-HAp) materials show an analogous chemical composition to the biogenic mineral component of calcified tissues and depending on their topography they may mimic the specific arrangement of the crystals in bone. In this work, we have evaluated the potential of four synthesized nano-HAp superstructures for the *in vitro* conditions bone-repair. Experiments are underway to investigate the effects of the material microstructure, surface roughness and hydrophilicity on their osseo-integration, osteo-conduction and osteo-induction abilities. Materials were tested in the presence of both, rat primary osteoblast and rabbit mesenchymal stem cell. The following aspects are discussed: (i) cytotoxicity and material degradation; (ii) rat osteoblast spreading, proliferation and differentiation; and (iii) rabbit mesenchymal stem cell adhesion on nano-HAp and nano-HAp/ collagen type I coatings. We effectively prepared a material based on biomimetic HAp nano-rods displaying the appropriate surface topography, hydrophilicity and degradation properties to induce the *in vitro* desired cellular responses for bone bonding and healing. Cells seeded on the selected material readily attached, proliferated and differentiate, as confirmed by cell viability, mitochondrial metabolic

activity, alkaline phosphatase (ALP) activity and cytoskeletal integrity analysis by immunofluorescence localization of alpha-smooth muscle actin (α-SMA) protein. These results highlight the influence of material's surface characteristics to determine their tissue regeneration potential and their future use in engineering osteogenic scaffolds for orthopedic implants.

1. Introduction

Current options related to bone injury therapies such as auto-grafts, allo-grafts and a variety of synthetic or biomimetic devices are unsatisfactory. The evidence base is the existence of significant limitations including the need for additional surgeries, morbidity associated with the donor site, limited material supply and inadequate size or shape of the implantable donor tissue. [1, 2] All those limitations lead to the development of advanced approaches to assist the skeletal tissue's reparation and reconstruction; avoiding the requirement of a permanent prosthesis. [3-5] Overcoming these challenges requires not only that the engineered substitute has both structural resemblance with the native tissue and ability to perform similar biological functions, but also it has to avoid problems of donor site scarcity, immune rejection and pathogen transference.[6-9] In addition, a bone substitute should ideally degrade at an equivalent rate to tissue regrowth.[7] In this regard, nanosized hydroxyapatite (nano-HAp) materials has been widely investigated for many biomedical applications related to calcified tissues, i.e., bone and dental composite fillers,[10, 11] maxillofacial reconstruction and augmentation,[12, 13] tissue engineering scaffolding[14-16] and coatings for metallic orthopedic prosthesis.[17] The main reason is that nano-HAp mimics the natural chemical composition and dimensions of mineralized phase found in the extracellular matrix (ECM) of bone.[18] The most significant advantages of nano-HAp powders compared to coarse synthetic crystals are their enhanced sinterability and densification, better osteo-conductive and osteo-inductive capabilities, and improved fracture toughness as a consequence of their grater surface area.[19] However, despite of these valuable properties, the effect of nano-HAp properties on tissue response has not yet been fully understood.[20] When a biomaterial is introduced into a living tissue, the ensuing biocompatibility and the host responses depends on their physical and chemical properties that promote the initial reactions of cells upon the material surface.[20, 21] In such terms, it was determined that the material's surface roughness is closely related to the extent and strength of cell's adhesion, proliferation and differentiation; subsequently to the material's osteo-induction, osteo-conduction and osseo-integration, thereby

the bone repair abilities. The microstructure and topology of nanostructured materials depend on their synthesis method, as well as on their processing conditions; a minor change in the powder compaction or in the sintering conditions can result in a variety of different porosity characteristics.[22] Consequently, it is extremely important to select the most appropriate technique when formulating nano-materials with desired properties combinations. In a previous work, we prepared four hydroxyapatite materials templated by different micelle-polymer structured networks.[23] The synergistic interaction of each polymer in contact with Hexadecyl-trimethyl ammonium bromide (CTAB) rod-like micelles results in crystalline HAp nano-rods of 25-50 nm length organized in hierarchical structures with different roughness and porosity. The role of material's surface texture was revealed as a key factor in the nucleation and growth of a bone-like apatite coating in contact with simulated body fluid (SBF); an essential requirement to estimate the materials' bone-bonding and osseo-integration potential.[24, 25] The growing of the different structures is attributed to a dissimilar matching of crystal planes in the material and in the apatite layer formed. In specific synthesis conditions, a biocompatible material with a Ca/P ratio close to that exists in the trabecular bone and, a morphology that are considered essential for bone-bonding was obtained.[23] Since the roughness, morphology and micro-patterning of the four investigated nano-HAp superstructures are crucial points for their optimal osseo-integration capabilities, the aim of this study was to carry out an *in vitro* evaluation of the effect of these parameters to induce the desired bone repair cellular responses, i.e. osteo-induction and osteo-conduction abilities. The effects of the synthesized materials' surface characteristics on the following factors are discussed: (i) nano-HAp material degradation and cytotoxicity; (ii) rat osteoblast spreading, proliferation and differentiation; and (iii) rabbit mesenchymal stem cell adhesion, mitochondrial metabolic activity, and spreading when cultured on surfaces coated with HAp nanoparticles and fibrillar collagen type I.

The results of this study were expected to serve as a reference in the selection and/or in the manufacturing of the proper nano-HAp materials' surface characteristics to maximize their bone-repair properties.

2. Materials and methods

2.1 Materials

Hexadecyl-trimethyl ammonium bromide (CTAB, MW = 364.48 g mol^{-1}, 99% Sigma-Aldrich); poly(ethylene glycol) 400 (PEG 400, Sigma-Aldrich, MW = 380–420 g mol^{-1}, δ = 1.126 g/mL at 25 °C); poly (propylene glycol) (PPG, Sigma-Aldrich, MW = 425 g mol^{-1}, δ = 1.004 g/mL at 25 °C); poly(ethylene glycol) - block poly (propylene glycol) – block - poly(ethylene glycol) (PEG–PPG– PEG, PEG 10 wt.%, Sigma-Aldrich, MW = 2800 g mol^{-1}, δ = 1.018 g/mL); octylphenyl-polyethylene glycol (IGEPAL®CA 630, $(C_2H_4O)_nC_{14}H_{22}O$, Sigma-Aldrich, MW = 603 g mol^{-1}, δ = 1.06 g/mL at 25 °C); sodium phosphate (Na_3PO_4, MW = 148 g mol^{-1}, 96% Sigma-Aldrich); calcium chloride ($CaCl_2$, MW = 91 g mol^{-1}, 99% Sigma-Aldrich) and sodium nitrite ($NaNO_2$, MW = 69 g mol^{-1}, 97% Sigma-Aldrich) were used without further purification. Alpha-Minimum Essential Medium supplemented with 15% fetal bovine serum (α-MEM-15%FBS, Sigma-Aldrich); ALP activity kit (Wiener lab., Rosario, Argentina), Xylazine (Rompun, CDMV, 20 mg/mL); Ketamine (Rogarsetic, CDMV, 100 mg/mL); sodium pentobarbital (Euthanyl) solution IV (CDMV, 240 mg/mL). Collagen type I from rat tail solution (3.9 mg/mL, Sigma-Aldrich); Dulbecco's Modified Eagle Medium: Nutrient Mixture F-12 (DMEM/F12, Gibco) with supplemented sodium bicarbonate (2.438g, Sigma-Aldrich); phosphate buffered saline (PBS without Ca/Mg, 1X, Sigma-Aldrich); paraformaldehyde ($HO(CH_2O)_nH$, Sigma-Aldrich); normal Goat Serum (Sigma-Aldrich); Triton X-100 (Sigma-Aldrich); Bovine Serum Albumin (BSA, Sigma-Aldrich); Alexa Fluor® 488 goat anti-mouse IgG (H+L) (Molecular Probes, 2 mg/mL); Mouse Monoclonal Anti-Actin, α-Smooth Muscle antibody (clone 1A4, Isotype IgG2a, Sigma-Aldrich, 1μg/mL); Hoechst 33342 (Gibco, 2 μg/mL); Fluoromount-G (Southern biotech); 3-(4,5-Dimethylthiazol-2-yl)-2,5-Diphenyltetrazolium Bromide (MTT, Sigma-Aldrich, 5mg/mL). For solution preparation, only triple-distilled water was used. For all experiments passage two to four (P2-P4) cells were used.

2.2 Bone - like HAp synthesis

Four HAp nanoparticles (7-9 nm diameter and 25-50 nm length) materials exhibiting different topographies and morphology were synthesized by a previously described methodology.[23] First, 350 mL of a 3.13 mM CTAB aqueous solution was mixed with 20 mL of PPG (MI), PEG (MII), PEG-PPG-PEG (MIII) or IGEPAL (MIV)[23] and stirred at 500 rpm during 10 minutes. Second, 200 mL of 2 M sodium nitrite aqueous solution and 2.2 g calcium chloride were incorporated in sequence. Finally, 200 mL of 0.14 M Na_3PO_4 aqueous solution was added to the above mixed

solution drop by drop at room temperature (RT) under magnetic stirring at 500 rpm. After the integration of all reactants, the solution was magnetically stirred for 1h. The resulting gels were left for 24 h in an autoclave at 100ºC. The obtained materials were filtered and washed with triplet-distilled water to remove impurities. Finally, surfactant was completely removed by calcination at 400°C during 3 h under air flux.

2.3 Near infrared spectroscopy

A Nicolet iS50 FTIR - NIR spectrophotometer (Thermo Scientific, Waltham, MA, USA) along with a diffuse reflectance accessory (DRA, also called an integrating sphere) was used to measure the reflectance properties of the powders. The spectra were obtained in air atmosphere and at RT. In the present study the integrating sphere was operated in the reflectance mode in the region of 1000 – 2500 nm. A Gold NIR Diffuse Reflection Standard (99.9% Reflective) was used as a reference to calibrate the baseline. The powder samples were supported inside flat bottom glass vials to form pellets of 10 mm diameter and 5 mm thick for measurements.

2.4 *In vitro* biodegradability under acidic conditions.

Assuming that the local pH around the ruffled border of osteoclasts is from 4.0 to 5.0 during the bone remodeling period,[26] *in vitro* degradation behavior of HAp particles under acidic conditions was evaluated by soaking them in an acetic acid/sodium acetate buffer solution (AcOH buffer) with a pH of 4.24 according to the method of Matsumoto *et al*. [27] HAp particles (200 mg) were soaked in 100 ml of the AcOH buffer solution at 25ºC and 36ºC for 3, 12, 16 and 25 days. The degradability of nano-HAp materials was estimated from the rate of weight loss (W_L) accordingly to Tampieri *et al.:* [16]

$$\%W_L = \frac{(W_0 - W_t)}{W_0} \times 100$$

where W_0 and W_t are the dry weights of the initial and the degraded specimens at different immersion times, t, respectively. The same procedure was followed under pH 7.4 (PBS) as a control.

2.5 Rat osteoblast isolation, culture and treatment

Calvarial osteoblasts were obtained from 5-day-old neonatal rats as previously described [23] and the cells were frozen in liquid nitrogen until their use. For the experiment, cells were cultured at 37 °C in α-MEM-15%FBS, 1% penicillin and streptomycin (P-S) under humidified air (5.5% CO_2). After 24 h, the medium was replaced by α-MEM supplemented with 10% (FBS) and 1% (P-S), and the cells were cultured until ~80% of confluence (2–3 days). Calvarial osteoblasts were seeded in 48-well plates in the presence or the absence of the nano-particles (71.42 μg/ml) and cultured for 4 and 7 days in α-MEM-10% (FBS)-1% (P-S), in a humidified atmosphere (5.5% CO_2) at 37 °C. It is known that the presence of calcium in the culture media stimulate osteoblast differentiation,[28] therefore the cells were cultures in presence of 4 mM of $CaCl_2$ as positive control.

2.6 Alkaline phosphatase activity in rat osteoblast

After cells treatments, the ALP activity was measured in lysed primary rat osteoblasts as it was descript by Ayala – Peña *et al.* [29] The ALP activity was estimated using a commercially available kit and indirectly measured by the amount of phenol released; the results were based on the increase in absorbance at optical density (OD) 520 nm. A blank (B) and a standard (S) (200 IU/l phenol) were also processed. Optical density of the samples (D) was measured and ALP activity was calculated as follows:

$$ALP\left(\frac{IU}{l}\right) = \frac{200\ IU/l \times (D - B)}{(S - B)}$$

2.7 Rabbit mesenchymal stem cells (MSCs) isolation

All protocols involving animals were approved by institutional ethics committees. MSCs were obtained form 9-11 month old New Zealand White rabbits which were sacrificed under Xylazine-Ketamine induced anesthesia using 150 mg/kg sodium pentobarbital (Euthanyl) solution IV. Bone fragments from the subchondral bone of the distal femur were submitted to collagenase digestion to release cells from marrow stroma that were pelleted, and deposited in petri dishes in complete culture media, DMEM/F12+10%FBS+1%P-S, in a humidified 5% CO_2 incubator. The obtained cells were cultured for 5 days during which the media was changed every 2 days to

remove non–adherent cells and to select for adherent cells. The primary MSCs were cryopreserved at P0 and at P1, then thawed and passaged for the cell assays.

2.8 Adhesion assay

2.8.1. Rabbit MSCs metabolic assay on nano-HAp coatings

Viable MSCs with active metabolism reduce MTT into a purple colored formazan product that can be solubilized and quantified by spectrophotometric means. When cells die, they lose the ability to convert MTT into formazan, thus color formation serves as a marker of only the metabolically active cells.[30, 31] Therefore, this assay was performed with the objective to evaluate the MSC metabolic activity in wells coated with the four different nano-HAp materials (MI, MII, MIII and MIV) and indirectly their viability.[31] For sterilization, nano-HAp materials were autoclaved 30 min at 120°C. Then a water material dispersion was prepared by placing the components on a rotating mixer for 5 min. Following, a 96-well plate (0.32 cm^2 / well) was filled with increasing amounts of nano-HAp material dispersions to have a final coating of 15 - 3100 µg HAp/cm^2. Finally, the material-coatings were allowed to dry overnight on shaker in a biological safety cabinet to obtain a homogeneous dry-coat surface on the bottom of the well. MSCs were seeded at a density of 10,000 cells per well and were cultured in pre-coated culture plate during 24h and 48h in complete culture media (DMEM/F12+10%FBS+1%P-S). The homogeneous distribution and attachment of HAp nanoparticles on the bottom of the wells, before and after MSCs seeding, was checked by optical microscopy; see figure 6 ESI. Pre-coated wells with medium and no cells were used as negative controls (C -) and uncoated wells were used as positive controls (C +). The MTT solution was added in each well at 0.5 mg/mL final concentration and the plate was incubated during 3h under humidified air (5% CO_2). The wells were aspirated and 100% DMSO (200 µL) was added and the resulting formazan was quantified using an ELISA plate reader (OD 570). The absorbance of coated wells without cells was used as blanks.

2.8.2 Rabbit MSCs metabolic assay on nano-HAp (MI) / collagen type I (Co I) coating

Rabbit MSCs adhesion and metabolic activity under four different MI/Co I weight ratios coating conditions were studied (MI/Co I: 0/1; 0.5/1; 1/1 and 2/1, with Co I = 31µg/cm^2); for this a MTT assay was done in a 96-well plate as it was described above. To prepare MI/ Co I coatings, the

commercial rat tail collagen - acetic acid (20 mM) solution was neutralized with a 20 mM NaOH solution. Then, three different concentrations of MI water dispersions were prepared and mixed with the properly amount of Co I neutral solution to obtain the different MI/Co I weight ratio coatings. Finally, the solutions were allowed to bind into the well plate by a dry – coating process (see point 2.8.1). Adhesion of MSCs on non-coated wells was used as control.

2.8.3. MSC actin-based spreading on collagen type I with and without nano-HAp: Immunofluorescence confocal microscopy

The cytoskeleton is known to play a key role in the mechano-transduction steps, and it can also contribute to MSC differentiation.[32] Multipotential mesenchymal stem cells also express α-smooth muscle actin (αSMA), and actin stress fibers can be used to demonstrate cell attachment responses. This experiment tested the hypothesis that MSCs attach and spread on collagen type I incorporated with nano-HAp. 10,000 rabbit MSCs/well were seeded in individual Culture Slide (Falcon®, Corning) glass chambers dry-coated with Co I or MI-Co I, as described above. Non-coated glass slide chambers were used as a C+. Cells were incubated for 29 h in a humidified cell culture incubator with 5% CO_2, then fixed with 4% paraformaldehyde for 5 min and then washed three times for 5 min with PBS. They were blocked and permeabilized with 20% v/v Goat serum/PBS/0.1% TritonX100 for 15 min at RT. After washing with 1% BSA/PBS/0.1% TritonX100 for 5 min the cells were incubated with primary antibody anti α-SMA (clone 1A4, Isotype IgG2a, Sigma-Aldrich) diluted to 1μg/mL in 1% BSA/PBS/0.1% TritonX100 for 30 minutes at RT. Subsequent to three washes with 1% BSA/PBS/0.1% TritonX100 for 10 min the glass slides were incubated with secondary anti-mouse antibody conjugated with Alexa 488 diluted to 1.3 μg/mL in 1% BSA/PBS/0.1% TritonX100 for 30 minutes at RT. After two 10 min PBS washes a counter stain was done with Hoechst 33342 diluted to 2μg/mL in PBS for 1 min at RT. The slides were washed two times with PBS for 10 min. Finally, the slides were separated from the chamber and Fluoromount-G was used to mount the slides. They were covered with aluminum foil and kept to dry for 24h. Images were acquired using Olympus FluoView™ FV1000 laser scanning confocal microscope with laser operational wavelength set at 405 nm for blue signal with Hoechst counterstain in cell nucleus and at 488 nm for green signal for α-SMA expression. All images were analyzed with help of the software Image J (National Institutes of Health, Bethesda, MD). Cell number was determined by count of nucleus positive for Hoechst

stain in a histology field per sample, and α-SMA expression was quantified from total green pixels per image with the data calculated as a percentage of (green pixels per image)/(total pixels). In addition, α-SMA expression was characterized by the mean brightness value of green pixels determined from the intensity of all green pixels per field in monochromatic images of the laser set at 488 nm (see **figure 10 ESI** of the electronic supporting information (ESI)).

2.9 Statistical analysis

All quantitative tests were carried out at least in triplicate, and then mean values with standard deviations were calculated. Statistical analysis of data was accomplished by one factor analysis of variance (ANOVA). Student's *t*-test and probability values below 0.05 ($p < 0.05$) were considered significantly different. Quantitative data are expressed as mean ± standard deviation (SD) from the indicated set of experiments.

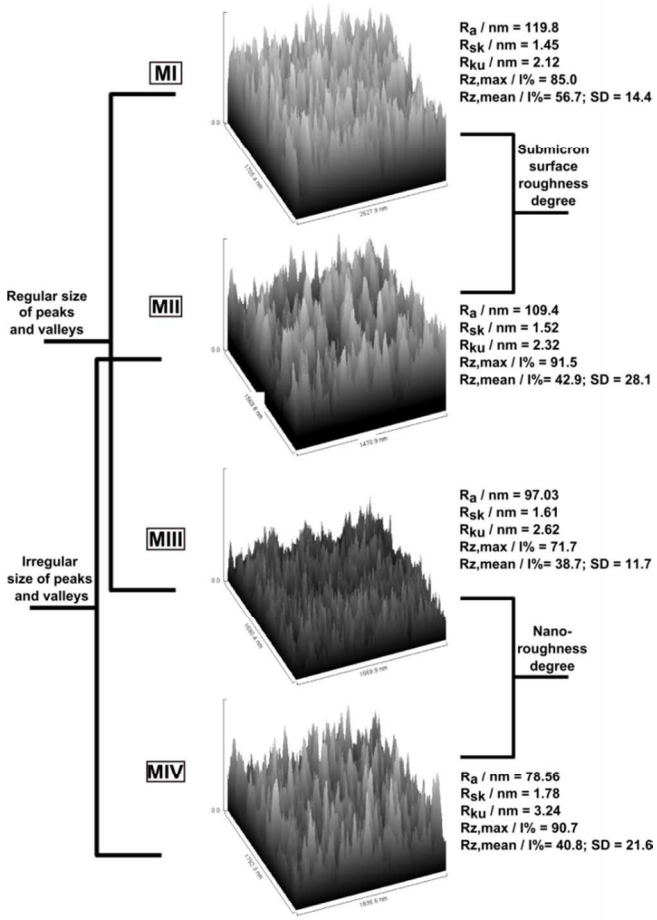

Figure 1: 3D surface plots of nano-HAp materials. Percentage of intensity (I%); Standard deviation (SD).

3. Results and discussion

Osteo-induction, osteo-conduction and osseo-integration are interrelated and are the required abilities of a bone-healing material.[33] Osteo-induction implies the recruitment of immature cells and the stimulation of these cells to develop into mature osteoblast; this process is part of normal bone healing and is responsible for the majority of newly formed bone after a fracture or an implant insertion. Osteo-conduction means that bone grows on a surface; is a term usually used in conjunction with implants. Osseo-integration is the stable anchorage of an implant achieved by direct bone-to-implant contact. Osteo-conduction and osseo-integration both depend not only on biological factors, but also on their response to the presence of a foreign material. [33] The effect of nano-HAp powder's surface topography, hydrophobicity and degradation on their *in vitro* osteo-induction, osteo-conduction and osseo-integration capacity is analyzed in the following sections.

3.1 nano-HAp powder's surface topography and hydrophilicity

Surface roughness degree, determined by the roughness arithmetical average deviation (R_a), can be distinguished according to the scale of the irregularities of the material surfaces: (i) surface macro-roughness, ≥100 μm; (ii) microscale surface roughness, from 1 to 100μm; (iii) submicron surface roughness, from 100 nm to 1 μm; and (iv) nano-roughness, ≤ 100 nm.[34] Each type of surface roughness has a specific influence on the behavior of the implant and also on the adhering cells.[34] In a previous work[23], by means of digitalized scanning electron microscopy images and different software packages, we computed R_a; the root mean square roughness (R_q); the maximum height of peaks (R_p); the maximum depth of valleys (R_v); the maximum height of the profile (R_t); Kurtosis (R_{ku}) and Skewness (R_{sk}) coefficients for the studied nano-HAp materials. The results of this study indicate that controlling surface roughness is an efficient platform to manipulate the biomimetic bone-like apatite layer deposition, which is essential for the material osseo-integration.[23] From MI to MIV, the materials showed a decrease in the surface roughness degree. Accordingly to the obtained R_a values, MI and MII are associated to a submicron surface roughness and the MIII and MIV materials to a nano-roughness surface. A deep analysis of parameters R_a, R_{sk} and R_{ku} was performed and their correlation can be appreciated in the 3D surface plots of **figure 1**; denoting differences in the surface topography of each material. All materials presented positive values of the parameters R_{sk} and R_{ku} indicating the existence of an asymmetrical surface in relation to a theoretical mean plane that cuts the relief. Nevertheless,

such asymmetry is different in each material, a thoughtful analysis can be performed from the single roughness depth ($R_{Z,i}$); the maximum roughness depth ($R_{Z,max}$) and the mean roughness depth ($R_{Z,mean}$) parameters; [35] see ESI for statistical details. $R_{z,i}$ is the vertical distance between the highest peak and the deepest valley within a sampling length. The arithmetic mean value of the single roughness depths of consecutive sampling lengths is $R_{z,mean}$ and the largest single roughness depth within the evaluation length corresponds to $R_{z,max}$. MI and MIII showed the lower computed values of $R_{z,max}$ and, a $R_{z,mean}$ data displaying the lesser standard deviations (SD). These values are associated to regular surfaces formed by a great number of high peaks and depth valleys of comparable extent. The higher $R_{z,max}$ and SD values exhibited by MII and MIV are associated to irregular surfaces created by peaks and valleys of dissimilar dimensions.

Furthermore, cell adhesion and spreading are highly influenced by the materials' surface hydrophilicity[34] and the water-surface interaction.[36] An explanation for these results will be that the presences of oxygen-containing groups on wettable shells make the surface more susceptible to adsorption of adhesion-mediating ECM proteins. On wettable surfaces, these molecules are adsorbed in a more flexible form, which allows them to be reorganized by the cells and thus provide access for cell adhesion receptors to the adhesion motifs on the ECM proteins. Nano-HA powders hydrophilicity and wettability were analyzed by inspection of near-infrared (NIR) spectra of H_2O molecules adsorbed on material surfaces, **figure 2**. All materials present a similar pattern of bands ascribed to different states of physisorbed H_2O molecules on their surface, indicating hydrophilicity. Small adsorption bands could be observed at 1380 nm and 1880 nm that can be assigned to the combination of symmetric and asymmetric stretching ($\nu_1 + \nu_3$) vibrational modes of less hydrogen-bonded water molecules.[37] Broad bands centered at 1420-1450 nm and 1920 nm are assigned to the ($\nu_1 + \nu_3$) and the combination of bending and asymmetric stretching ($\nu_2 + \nu_3$) vibrational modes of intermediate intensity hydrogen bonded water molecules.[37] Finally a broad, less intense band at 2200 nm similar to that due to the ($\nu_2 + \nu_3$) vibration modes of the ice[37] can be associated with highly structured hydrogen bonded water molecules. Ordered and strongly adsorbed hydration layers on HAp surfaces have been detected in literature reports.[38, 39] Experiments performed by Corno and co-workers[38] revealed that HAp surface-water binding energy originates by the direct interaction of the exposed Ca^{2+} with H_2O molecules, which simultaneously involves slightly strong H-bonds with the basic oxygen of the

PO_4^{-3} surface groups. At higher H_2O adsorptions, the lateral H-bonding interactions among the adsorbed molecules provide a significant fraction of the binding energy.

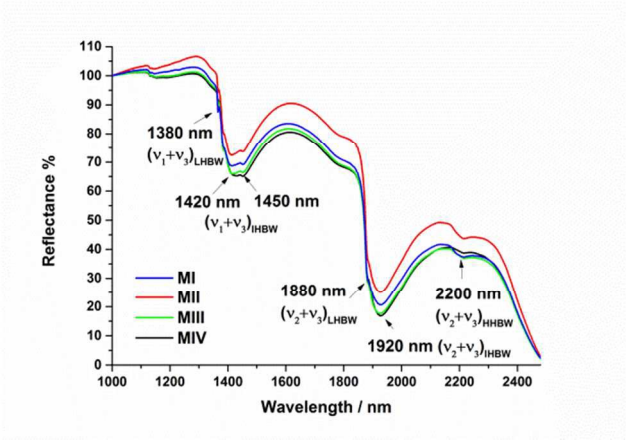

Figure 2: Near-infrared (NIR) spectra of H_2O molecules adsorbed on material surfaces. ν_1: symmetric stretching; ν_2: bending; ν_3: asymmetric stretching; LHBW: less hydrogen bonded water; IHBW: intermediate hydrogen bonded water; HHBW: high hydrogen bonded water.

3.2 nano-HAp powder's biodegradability

Under certain clinical situations, rapid resorption was reported to lead a lower quality of bone formation. Nevertheless for some applications, such as cranioplasty, rapid implant resorption and replacement by health tissue is perhaps not as important as implant stability or integrity. For others uses, such as periodontal bone defect repairs or sinus augmentation; the ability of the implant to be replaced quickly by bone is highly desirable.[40] These observations suggest that in order to achieve the optimal clinical results for each instance, the appropriate resorption rate of the implantable material must be carefully assessed. The *in vitro* degradation of nano-HAp materials, incubated at 25 and 36 °C, in physiological fluid environment (pH = 7.4) and under cell-mediated acidic conditions (pH = 4.24) was monitored by the material weight loss (W_L) as a function of time during a 25 days period. At acidic conditions and 25°C, **figure 3A**, materials are 50% degraded during the first 4-8 days of treatment. By completion of the evaluation period, materials had shown a maximum degradation of 64-70%. Increases of temperature causes a considerably increase of the nano-HAp materials' degradation rate. As shown **figure 3B**, at 36°C the materials are 50% degraded at the first 1-2.5 days of treatment; showing 98-100% degradation on the 25th day.

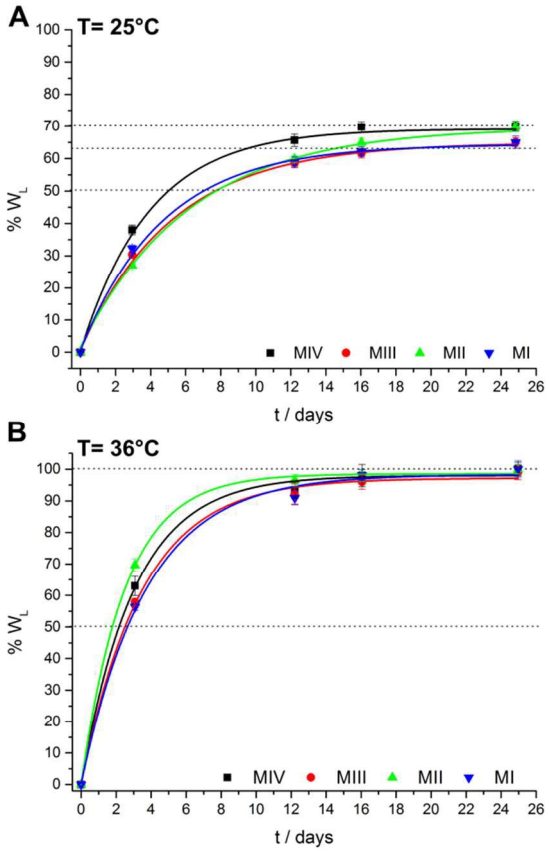

Figure 3: Degradation of nano-HAp materials at pH = 4.2 and different temperature conditions. (**A**) 25°C and (**B**) 36°C.

Many models have been already proposed to explain the processes involved in the dissolution of calcium apatites in acids.[41] They generally accepted that the steady-state conditions of apatite dissolution in aqueous acidic media include the following steps: (i) diffusion of chemical reagents (H^+ and acid ions) from bulk solution to the solid-liquid interface; (ii) adsorption of the H^+ and acid ions on the surface of apatite; (iii) chemical transformation on the surface; (iv) desorption of products (Ca^{2+}, PO_4^{3-} ions) from the surface; and (v) their diffusion into the bulk solution.[41] Literature findings[39] emphasize that after adsorption of water the exchange of Ca^{2+} by two H^+ is energetically favored; see section 3.1. Instantaneously after being placed in contact, water molecules and acid ions are adsorbed on the surface of apatite crystals forming a solid-liquid interface and various adjacent strata, such as a Nernst diffusion layer or an electrical double layer. Transport of the chemicals to the solid-liquid interface always happens by ionic diffusion through the Nernst diffusion layer. The thickness of this layer depends on both the

solution hydrodynamics and the dissolving crystal's dimensions. It decreases with the augment of solution's agitation and with reduction of the crystal's size.[41] In our experimental conditions, the thickness of the diffusion layer is reduced due to the use of nano-particles. However, in none of the cases the thickness becomes equal to zero and as a consequence a concentration gradient is always present near the solid-liquid interface; the diffusion laws always remain valid. All findings of the diffusion-controlled model remain applicable for any case of apatite dissolution which is consistent with an improved degradation at a superior temperature. The temperature's augment intensifies the thermal agitation of the ions in solution and therefore their diffusion through the Nernst's layer. A similar approach is correct for the surface phenomena; when dissolution occurs, adsorption and desorption of ions and water molecules, as well as, chemical transportation always take place on the surface regardless the experimental conditions chosen. Thus, surface properties of the materials can be very important. At both evaluated temperatures, the degradation profiles were similar for all materials, whereas at 36°C the initial degradation rate follows the resultant sequence: specimens MII > MIV > MIII > MI. Degradation rate is a function of the surface roughness parameters' set, **figure 4**. Comparing the degradation test's results with the 3D surface maps constructed based on the surface texture's values, it was observed that the faster degradation material (MII) is that which has a submicron rough surface composed by peaks and valleys of dissimilar dimensions; while the material exhibiting lower degradation rate (MI) has a submicron rough surface formed by a great number of high peaks and depth valleys of comparable extent. Materials MIII and MIV showed intermediate surface topographies between the aforementioned extremes and as a consequence intermediate degradation rates. No significant effect on materials' degradation can be appreciated by the variation of Ca/P ratio or the 3D fractal dimension (D_{3D}). Under a physiological fluid's environment at 25°C or 36°C, materials' degradation was not considerable; results are shown in **figure 5ESI**. This is a desirable characteristic because the biodegradation rate must be comparable to the formation of bone tissue, which is between an 8 to 16 weeks.[42]

This degradation study was carried out in absence of enzymes and cells, and therefore cannot be predictive of the resorption times *in vivo*; however an important *in vitro* result of the degradation analysis is that nano-HAp materials do not dissolve under pH physiological fluid conditions, yet are resorbable under cell-mediated acidic conditions[26] similar to those that are set *in vivo* during new bone formation[43, 44] and bone remodeling. The goal of this *in vitro* biodegradation study is to

ascertain that nano-HAp materials can act as temporary templates, providing structural and mechanical support initially and regenerative properties over time and finally, under resorption conditions, its completed degradation.

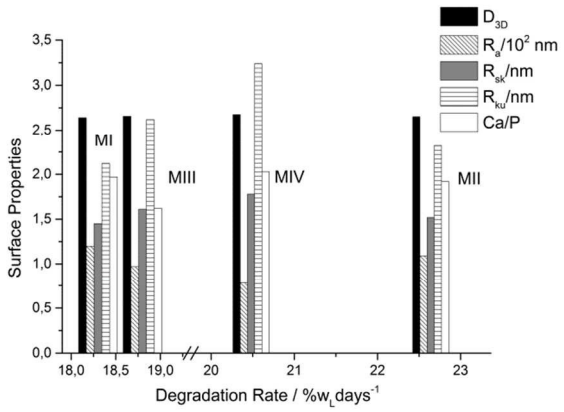

Figure 4: Variation of degradation rate versus the material's roughness parameters.

3.3 nano-HAp powder's osteo-induction, osteo-conduction and osseo-integration properties

Bone repair properties of nano-HAp powders were tested in the presence of two different cell types that could be potentially be used in orthopedic or tissue engineering applications:[45, 46] primary mature osteoblast and mesenchymal stem cells that are known to form bone tissues when implanted *in vivo* or differentiated into bone cells.[47]

3.3.1 Osteoblast spreading, proliferation and differentiation.

The variation of nano-HAp powders' surface topography and degradation on neonatal rat calvarial osteoblasts viability, spreading and morphology were preliminary analyzed by simply microscopic observation of cultured cells through two different treatments during 24, 48 and 72h, accordingly to previous work.[23] During a first procedure (T1), the nano-HAp powder was extended in the culture media and cells were seeded in the presence of the material from the beginning of the test. Then, a second treatment (T2) was applied to evaluate the effect of material on cells' spreading perturbation; at this time osteoblasts were plated in culture media and nano-HAp were added 24h later. The cells' behavior was similar to control after 72h for both treatments, **figure 5A**. To evaluate the cell's morphology, the samples were then smeared on a microscope slide, air dried, fixing with absolute ethanol and stained by Giemsa dye.[48] In the

presence of all tested nano-HAp samples, rat osteoblasts displayed normal morphological features[49] for both applied culture methods; they showed their typical polygonal or widespread forms with fine filopodia and abundant surface folds, **figure 5B**. The obtained results exclude any significant difference due to the nano-HAp powder surface properties or particle degradation on the process of adhesion, spreading and morphology of the tested cells. There are no apparent differences in the cell viability after they are cultured in the presence of the prepared materials. Further inspection of cell - material interactions, was analyzed by differentiation assays.

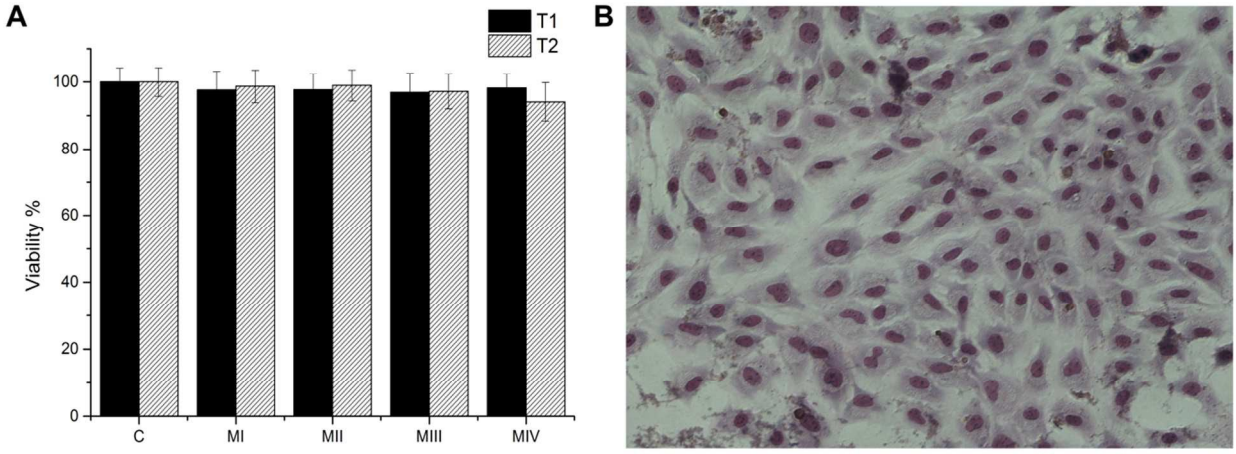

Figure 5: (**A**) Rat primary osteoblast viability after cultured through to two different treatments (T1 and T2) during 72h in the presence of different nano-HAp materials. (**B**) Giemsa stains of rat primary osteoblast after culture in the presence MI sample.

The induction of APL activity is used as a predictive parameter for *in vivo* osteoblast maturation. A successful bone scaffold must demonstrate support for enhanced bone formation, including organic and inorganic components of natural tissue. ALP is a key component of bone matrix vesicles because of its role in the formation of apatite calcium phosphate[50], and it is an early indicator of immature osteoblast activity. Although cells in several tissues (liver, kidney, placenta, etc.) generate the enzyme, elevated levels of ALP in bone tissue typically are observed several days prior to neo-mineralization and during the initial phase of bone matrix deposition.[51, 52] **Figure 6** displays the influence of different materials properties on the ALP activity of rat

primary calvarial osteoblast after 4 and 7 days of culture in synthetic serum substitute with and without the addition of 4mM Ca^{2+} ion concentration.

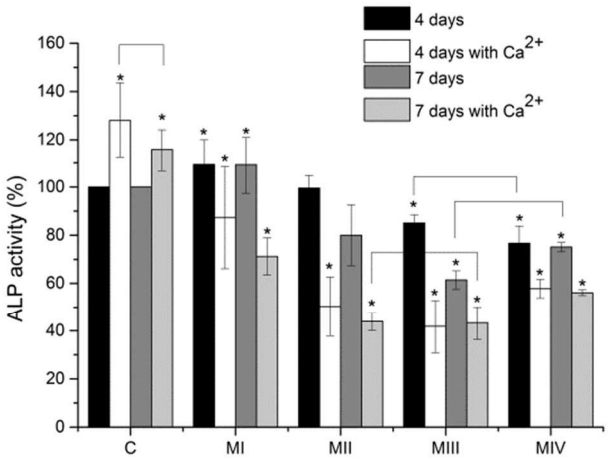

Figure 6: ALP activity of rat primary osteoblast after culture in the presence of different nano-HAp materials. [Ca^{2+}] = 4mM. Statistical analysis was performed between different materials and control, *$p < 0.05$; significant differences between the samples are indicated with brackets.

The material exhibiting a submicron rough surface composed by peaks and valleys of comparable extent (MI), shows an ALP activity statistically superior to the control during the 7 days of treatment ($p < 0.05$); while those materials having a surface composed by peaks and valleys of dissimilar dimensions (MII), nano-surface roughness degree (MIII) or both (MIV) present a considerable decrease in ALP activity that intensified with time. Investigations performed by Maeno *et al.*[28] revealed that low concentrations of Ca^{2+} (2 – 6 mM) can provide suitable conditions for osteoblast proliferation and differentiation in both monolayer and 3D cultures. Our experiments showed a clear decrease in rat calvarian osteoblast differentiation after the addition of 4mM Ca^{2+} in culture media in the presence of all tested nano-HAp materials, while in absence of the materials the ALP activity increases in respect to the control and in agreement with Maeno *et al.* results.[28] Statistically considerable and equivalent ALP activity reduction was noticed in the presence of materials MII, MIII and MIV. The obtained results may be associated with an increase of Ca^{2+} concentration due to nano-HAp degradation above the acceptable limit to promote cell differentiation. The pH of the interstitial fluid bathing cells tissues will generally slightly acid and subject to complex gradients, depending on the metabolic activity of the cells.[53]

Being MI the less degraded material in acid conditions, it presence generates the smaller reduction in ALP activity.

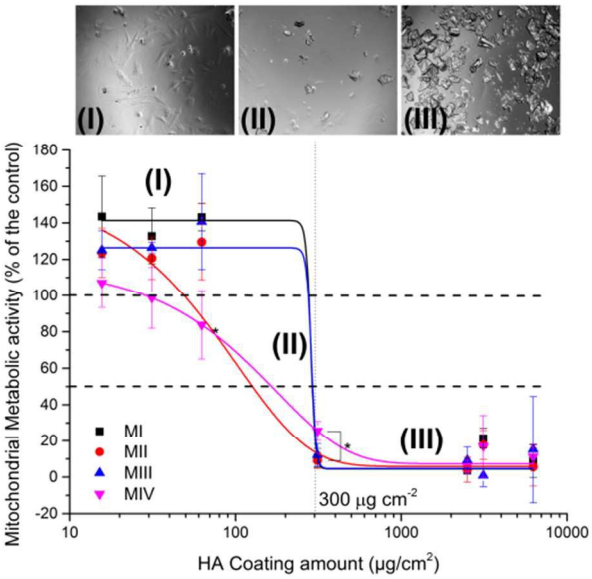

Figure 7: Mitochondrial metabolic activity of rabbit mesenchymal stem cells adhered on different concentration of nano-HAp materials coatings. Experimental results were fitted to Boltzmann Sigmoidal curve (continuous line); no-coated well was used as control. Statistical analysis was performed among different materials, *$p < 0.05$; significant differences between the samples are indicated with brackets. **Inset:** optical microphotographs of adhered cells on (I) 15μg cm^2, (II) 300μg cm^2 and (III) 3100μg cm^2 MI coating.

3.3.2 Effects of nano-HAp powders on MSCs adhesion

Rabbit MSCs spreading was evaluated on coatings of collagen type I, the principle organic component of bone, with and without incorporated nano-HAp. The experiments were performed in an attempt to mimic a remodeling bone environment in which the MSCs attach and differentiate. First, a cytocompatible level of nano-HAp to use in the coating was identified. Rabbit MSCs were treated with different amounts of nano-HAp particles (15 – 3100 μg HAp / cm^2 coating), and their mitochondrial metabolic activity was measured after culture for 24 and 48h. The obtained data collected after the first 24 hours were inconclusive, while by the completion of 48 hours the results show that the inhibition effect produced by the particles was dose- and material type-dependent, **figure 7**. Mitochondrial metabolic activity was correlated

with the cells viability; proliferation status was confirmed by microscopic observation, **figure 7 inset**; for more details see, **figure 6ESI**. A measurement of MSCs viability after adhesion is imperative to evaluate the capacity for a material to support initial cell spreading and proliferation. In order to be successful providing a scaffold with therapeutic potential, the cells must demonstrate viability properties statistically comparable to the control. As expected, our results suggest that cells viability is related to the materials surface properties. Materials having comparable dimensions of peaks and valleys on their surfaces (MI and MIII) exhibited a 50% cell proliferation inhibition at 300 μg HAp / cm^2 coating; while it was required 162 and 124 μg HAp / cm^2 to reach similar cell mortality in the presence of materials more asymmetrical surfaces (MII and MIV). The sample MIV, which has a combination of nano-surface roughness degree and an asymmetrical topography, causes the greatest toxic effect on initial MSCs viability. As the concentration of particles exceeded the 300 μg HAp / cm^2 coating, the inhibition effect is similar for all tested materials. Literature findings[54] inform that the degree of toxicity of nano-HAp powder correlated well with the degree of cellular uptake. This strongly suggests that cellular particle load is the main cause of cytotoxicity, probably due to the release of calcium.[54] This fact is consistent with our results since the less degraded material, MI, causes the lowest cytotoxicity of cells of mesenchymal origin.

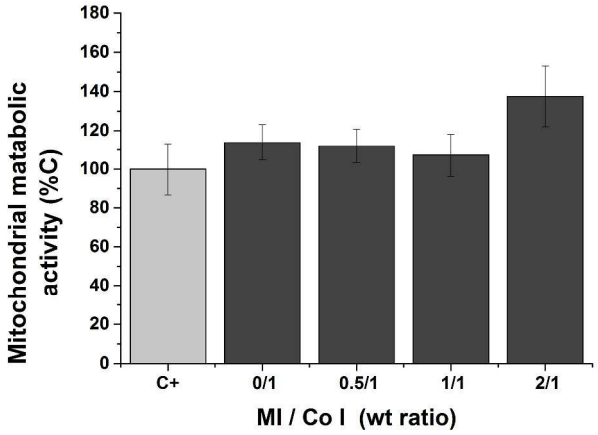

Figure 8: Mitochondrial metabolic activity of rabbit MSCs adhered on different MI/CoI weight ratio coatings. Non-coated wells were used as positive control (C+)

3.3.3 MSCs adhesion on a mimic bone matrix

Regarding to cell-material interactions, the information discussed in the preceding sections indicate a clear difference among sample MI and the rest of the studied nano-HAp superstructures. MI provides the adequate environment to permit rat primary osteoblast differentiation, and higher ALP activity relative to the control compared to the attained values in the presence of the other three materials. Even though there are no difference among rat primary osteoblast spreading and proliferation in the presence of the four tested nano-HAp powders, rabbit MSCs adhesion and viability on the MI coating is slightly favored in comparison to control at low material concentration. Furthermore, it is required a greater amount of MI material to reach the 50% of rabbit MSCs mortality. Results obtained in a previous work[23] showed that the mineral HAp coating formed on the surface of MI material after it was immersed in simulated body fluid (SBF) giving an estimate of the material's bone-bonding potential,[24, 25] exhibited a globular morphology and a Ca/P weight ratio of 1.56 close to what exists in trabecular bone.[55] Both characteristics are considered essential for bone-bonding.[55, 56] Accordingly, the specimen MI was selected as the material with the best osseo-integration, osseo-induction and osteo-conduction characteristics to be combined with collagen type I in MI /Co I coatings and to indirectly evaluate their potential use in bone tissue repair. It is considered that the average mineral content of bone tissue is within the range of 30 to 55 vol% or 50 to 75 wt%, and collagen is the principal organic matrix in bone,[57] thus the MI/Co I coatings were prepared in compliance of these proportions and taking into account that higher amounts of MI (> 300 $\mu g/cm^2$) tested as coatings caused the inhibition of MSCs' adhesion and metabolic activity, see **figures 6ESI, 7ESI** and **8ESI**. **Figure 8** shows the rabbit MSCs mitochondrial metabolic activities after culture in the presence of different MI/Co I weight ratios coatings. No significant statistical difference in respect to control was observed among the MSCs viability after adhesion on the different MI/CoI coatings. Current discoveries have recognized that mechanical properties of the cellular environment such as its rigidity, geometry, and external stresses play an imperative role in the definition of the cellular function and fate.[58] It has been shown that mechanical properties influence cell shape and orientation, regulate cell proliferation and differentiation and even govern the development and organization of tissues.[58] It is widely known that for most tissue cells the traditional picture of the cell as a lipid membrane that surrounds a liquid-like cytosol containing localized organelles is not relevant.[59] Adherent cells such as fibroblasts, neurons, endothelial cells, and bone cells, contain an actively regulated gel-like elastic cytoskeleton.[60] The

elastic nature of the cytoskeleton is important not only for the mechanical stability of the cell, but also for transmitting mechanical signals in the form of elastic stress and strain fields, from the environment, through the cytoskeleton and to the nucleus.[61]

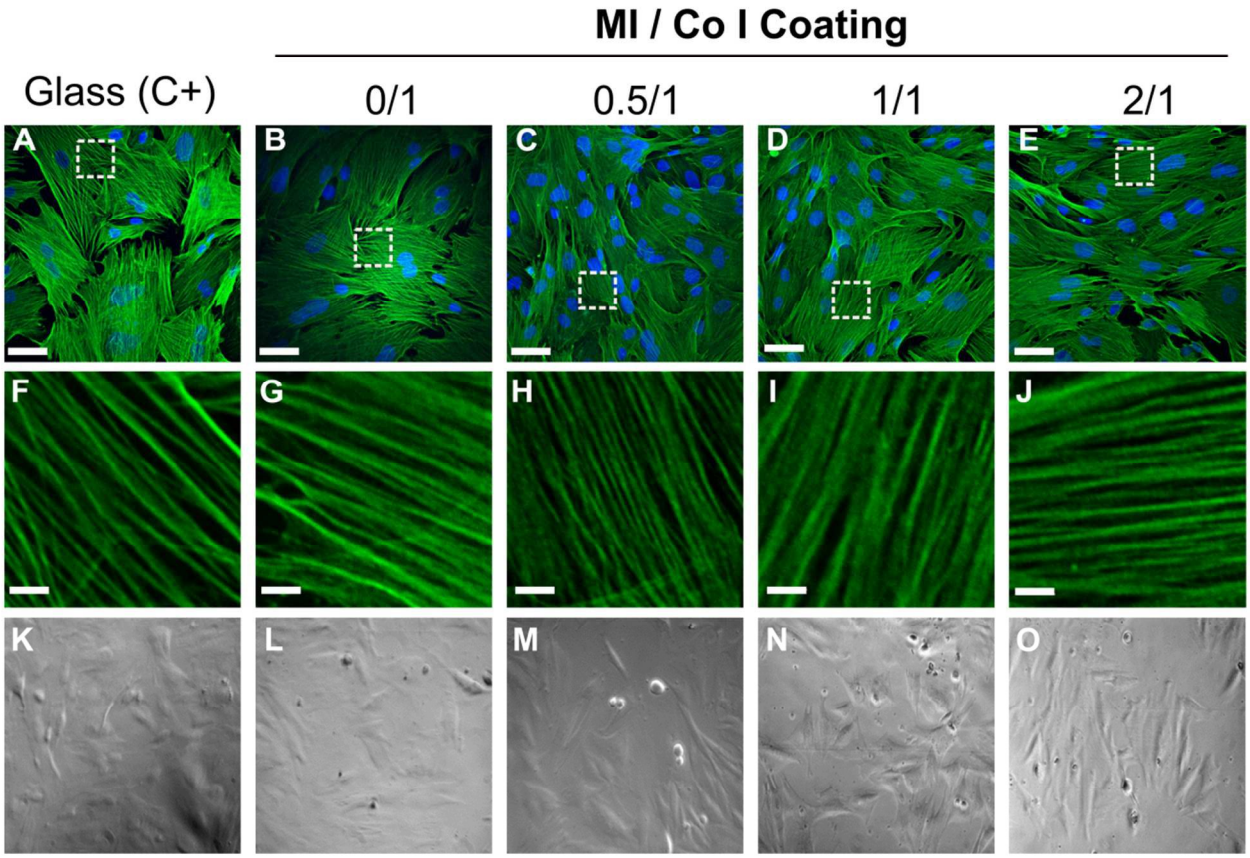

Figure 9: Immunofluorescence assay: (A-E) 40x magnification laser scanning confocal microphotographs showing cell nucleus and α-SMA expression, blue and green stains respectively, scale bar 50μm; (F-J) 400× magnification laser scanning confocal microphotographs showing α-SMA filaments' size and morphology, scale bar 5μm. (K-O) Optical phase contrast images showing MSCs' morphology and adherence to surface. Non-coated glass slide was used as positive control (C+).

The cytoskeleton is a complex dynamical network of actin, intermediate filaments, and microtubules that interact with a myriad of molecular motors and cross-linking proteins. Many of these proteins are collectively responsible for cellular mechano-sensing. Recent studies have identified a contractile muscle actin isoform, α-SMA, in osteoblasts[62] as well as in a number of

other musculoskeletal connective tissue cells. Associated studies demonstrated the ability of α-SMA-expressing osteoblastic cells to contract a collagen-glycosaminoglycan analog of extracellular matrix *in vitro*.[63] It was proposed that α-SMA enabled contraction might be responsible for the retraction of osteoblasts on the bone surface at the initiation of the remodeling cycle. Moreover, α-SMA -enabled contraction may allow for the generation of the higher forces required for the cellular modeling of the newly synthesized extracellular matrix, to impart the tissue specific architecture.[64] Thus, the elevation of α-SMA expression might be expected to be associated with an osteogenic process such as bone transport.[65] Furthermore, the α-SMA expression is a relatively reliable indicator that the MSCs cells maintain their mesenchymal stem cells phenotype.[66] MSCs' α-SMA-based spreading on MI/CoI coatings was evaluated by confocal fluorescence microscopy and histomorphometry.

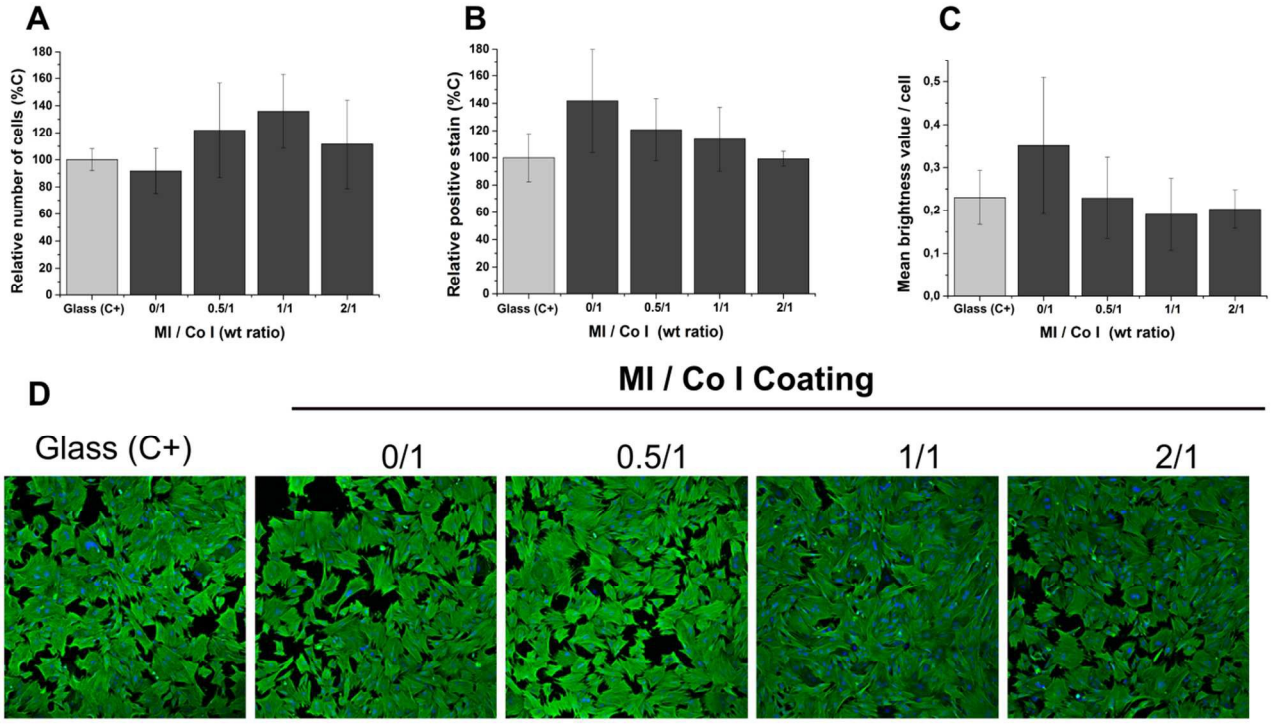

Figure 10: (A) Relative percentage of MSCs on cultured surface. **(B)** Relative percentage of positive stain for α-SMA. **(C)** Mean brightness value per cell and, **(D)** confocal microphotographs in order to show the α-SMA expression of MSCs adhered on different MI /Co I weight ratio coatings per cell. No-coated glass slide was used as positive control (C+).

Results indicate that the rabbit MSCs spread, adhere, and proliferate on 0.5/1, 1/1 and 2/1 MI/Co I coatings cultured in proliferation medium for 29h in the same manner as on biocompatible glass control surfaces exhibiting α-SMA filaments of similar size and morphology, **figure 9**. During the time analyzed, the visualization of the cell number and the rearrangement of the α-SMA's cytoskeleton do not shown any significant difference respect to control, **figures 10A-C**. The visual inspection of proliferation, as well as a measurement of cellular metabolism and spreading provided information on the ability of cells to populate MI/Co I coatings. Altogether, these data demonstrate that, in the conditions tested, *in vitro* culture MI/Co I materials are cytocompatible, and that the HAp nanoparticles does not interfere with mesenchymal stem cell character or spreading.

Conclusion

We successfully fabricated a biocompatible nano-HAp superstructure that possesses the precise controlled surface topography and hydrophilicity allowing normal growth and differentiation of bone cells *in vitro*. The material has a regular sub-micron rough surface and the optima degradation rate under cell-mediated acidic conditions, which resulted in a uniform cell seeding, spreading, adhesion and differentiation.

The obtained results highlight the importance of micro-patterning and surface properties of nano-HAp superstructures and provide new insight for the design of scaffolds based on HAp nanoparticles for effective bone repair and regeneration.

Acknowledgements: The authors acknowledge Universidad Nacional del Sur (PGI 24/Q064), Concejo Nacional de Investigaciones Científicas de la República Argentina (CONICET, PIP 11220130100100CO) and the Canadian Institutes of Health Research (CIHR, MOP 303615 to CDH). Also they acknowledge Sylvie Taillon for technical contributions. NLD and JL have doctoral fellowships of CONICET; GES and PVM are independent researchers of CONICET. NLD thanks the Emerging Leaders in the Americas Program (ELAP).

Electronic Supplementary Information (ESI) available: Calculation of roughness parameters R_z, $R_{z,max}$, and $R_{z,\ prom}$. Nano-HAp powders degradation after immersion in phosphate buffer (pH = 7.4). Optical phase contrast microphotographs of MSCs adhesion on nano-HAp and nano-

HAp/Co I coatings at different concentrations. Laser scanning confocal microphotographs of MSCs' α-SMA expression spreading on large amounts of nano-HAp (MI) coatings. Immunofluorescence microphotographs analysis by image software.

References

1. A. J. Salgado, O. P. Coutinho and R. L. Reis, *Macromol. Biosci.*, 2004, **4**, 743-765.
2. W. L. Fodor, *Reprod. Biol. Endocrinol.*, 2003, **1**, 102-102.
3. W.-J. Li, R. Tuli, X. Huang, P. Laquerriere and R. S. Tuan, *Biomaterials*, 2005, **26**, 5158-5166.
4. M. D. Kofron, X. Li and C. T. Laurencin, *Curr. Opin. Biotechnol.*, 2004, **15**, 399-405.
5. Y. Shandalov, D. Egozi, J. Koffler, D. Dado-Rosenfeld, D. Ben-Shimol, A. Freiman, E. Shor, A. Kabala and S. Levenberg, *Proc. Natl. Acad. Sci. U. S. A.*, 2014, **111**, 6010-6015.
6. L. Zhang and T. J. Webster, *Nano Today*, 2009, **4**, 66-80.
7. V. J. Shirtliff and L. L. Hench, *J. Mater. Sci.*, 2003, **38**, 4697-4707.
8. C. J. Koh and A. Atala, *J. Am. Soc. Nephrol.*, 2004, **15**, 1113-1125.
9. L. L. Hench and J. M. Polak, *Science*, 2002, **295**, 1014-1017.
10. M. Sadat-Shojai, M. Atai, A. Nodehi and L. N. Khanlar, *Dent. Mater.*, 2010, **26**, 471-482.
11. H.-W. Kim, H.-H. Lee and J. C. Knowles, *J. Biomed. Mater. Res., Part A*, 2006, **79A**, 643-649.
12. E. Neovius and T. Engstrand, *J. Plast. Reconstr. Aesthet. Surg.*, 2010, **63**, 1615-1623.
13. D. W. Lee, J. Y. Kim and D. H. Lew, *J. Craniofac. Surg.*, 2010, **21**, 1084-1088.
14. H. Wang, Y. Li, Y. Zuo, J. Li, S. Ma and L. Cheng, *Biomaterials*, 2007, **28**, 3338-3348.
15. S. J. Hollister, *Nat Mater*, 2005, **4**, 518-524.
16. A. Tampieri, M. Iafisco, M. Sandri, S. Panseri, C. Cunha, S. Sprio, E. Savini, M. Uhlarz and T. Herrmannsdörfer, *ACS Appl. Mater. Interfaces*, 2014, **6**, 15697-15707.
17. A. K. Lilikakis, S. L. Vowler and R. N. Villar, *Orthop. Cli. North Am.*, 2005, **36**, 215-222.
18. C. Liang, M. M. Joseph, C. M. L. James and L. Hao, *Nanotech.*, 2011, **22**, 105708.
19. S. V. Dorozhkin, *Acta Biomater.*, 2010, **6**, 715-734.
20. D. D. Deligianni, N. D. Katsala, P. G. Koutsoukos and Y. F. Missirlis, *Biomaterials*, 2001, **22**, 87-96.
21. H.-H. Huang, C.-T. Ho, T.-H. Lee, T.-L. Lee, K.-K. Liao and F.-L. Chen, *Biomol. Eng.*, 2004, **21**, 93-97.
22. H. Gleiter, *Acta Mater.*, 2000, **48**, 1-29.
23. N. L. D'Elía, A. N. Gravina, J. M. Ruso, J. A. Laiuppa, G. E. Santillán and P. V. Messina, *Biochim. Biophys. Acta, Gen. Subj.*, 2013, **1830**, 5014-5026.
24. T. Kokubo, H. Kushitani, S. Sakka, T. Kisugi and T. Yamamuro, *J. Biomed. Mat. Res.*, 1990, **24**, 721-734.
25. M. Bohner and J. Lemaitre, *Biomaterials*, 2009, **30**, 2175-2179.
26. R. Baron, L. Neff, D. Louvard and P. J. Courtoy, *J. Cell Biol.*, 1985, **101**, 2210-2222.
27. T. Matsumoto, M. Okazaki, M. Inoue, S. Yamaguchi, T. Kusunose, T. Toyonaga, Y. Hamada and J. Takahashi, *Biomaterials*, 2004, **25**, 3807-3812.
28. S. Maeno, Y. Niki, H. Matsumoto, H. Morioka, T. Yatabe, A. Funayama, Y. Toyama, T. Taguchi and J. Tanaka, *Biomaterials*, 2005, **26**, 4847-4855.
29. V. B. Ayala-Peña, L. A. Scolaro and G. E. Santillán, *Exp. Cell Res.*, 2013, **319**, 2028-2036.
30. N. J. Marshall, C. J. Goodwin and S. J. Holt, *Growth. Regul.*, 1995, **5**, 69-84.
31. Riss TL, Moravec RA, Niles AL, Benink HA, Worzella TJ and M. L, ed. C. N. Sittampalam GS, Nelson H, Eli Lilly & Company and the National Center for Advancing Translational Sciences; 2004-. Available from: http://www.ncbi.nlm.nih.gov/books/NBK144065/, 2013.
32. A. D. Bershadsky, N. Q. Balaban and B. Geiger, *Annu. Rev. Cell Dev. Biol.*, 2003, **19**, 677-695.

33. T. Albrektsson and C. Johansson, *Eur. Spine J*, 2001, **10**, S96-S101.
34. L. Bacakova, E. Filova, M. Parizek, T. Ruml and V. Svorcik, *Biotechnol. Adv.*, 2011, **29**, 739-767.
35. K. J. Stout, *Mater. Des.*, 1981, **2**, 260-265.
36. B. Kasemo, *Surf. Sci.*, 2002, **500**, 656-677.
37. M. Takeuchi, G. Martra, S. Coluccia and M. Anpo, in *Environmentally Benign Photocatalysts*, eds. M. Anpo and P. V. Kamat, Springer New York, 2010, ch. 22, pp. 527-542.
38. M. Corno, C. Busco, V. Bolis, S. Tosoni and P. Ugliengo, *Langmuir*, 2009, **25**, 2188-2198.
39. R. Astala and M. J. Stott, *Phys. Rev. B*, 2008, **78**, 075427.
40. L. C. Chow, *Dent. Mater. J.*, 2009, **28**, 1-10.
41. S. V. Dorozhkin, *World J. Methodol.*, 2012, **2**, 1-17.
42. M. R. Urist, *Science*, 1965, **150**, 893-899.
43. L. G. Raisz, *Clin. Chem.*, 1999, **45**, 1353-1358.
44. U. Kini and B. N. Nandeesh, in *Radionuclide and Hybrid Bone Imaging*, eds. I. Fogelman, G. Gnanasegaran and H. van der Wall, Springer Berlin Heidelberg, 2012, ch. 2, pp. 29-57.
45. P. Bianco and P. G. Robey, *Nature*, 2001, **414**, 118-121.
46. M. M. Stevens and J. H. George, *Science*, 2005, **310**, 1135-1138.
47. H. Petite, V. Viateau, W. Bensaid, A. Meunier, C. de Pollak, M. Bourguignon, K. Oudina, L. Sedel and G. Guillemin, *Nat. Biotech.*, 2000, **18**, 959-963.
48. G. Giemsa, *Zentabl. Bakteriol. Parasitenkd. Infectkrankh*, 1904, **37**, 308.
49. T. M. Lee, R. S. Tsai, E. Chang, C. Y. Yang and M. R. Yang, *J. Mater. Sci.: Mater. Med.*, 2002, **13**, 341-350.
50. H. C. Anderson, J. B. Sipe, L. Hessle, R. Dhamyamraju, E. Atti, N. P. Camacho and J. L. Millán, *The Am. J. Pathol.*, 2004, **164**, 841-847.
51. F. Liu, L. Malaval and J. E. Aubin, *J. Cell Sci.*, 2003, **116**, 1787-1796.
52. C. Heinemann, S. Heinemann, A. Bernhardt, H. Worch and T. Hanke, *Biomacromolecules*, 2008, **9**, 2913-2920.
53. T. R. Arnett, *J. Nutr.*, 2008, **138**, 415S-418S.
54. M. Motskin, D. M. Wright, K. Muller, N. Kyle, T. G. Gard, A. E. Porter and J. N. Skepper, *Biomaterials*, 2009, **30**, 3307-3317.
55. P. S. Vanzillotta, M. S. Sader, I. N. Bastos and G. de Almeida Soares, *Dent. Mater.*, 2006, **22**, 275-282.
56. T. Kokubo, H. Kushitani and Y. Ebisawa, eds., *Apatite formation on bioactive ceramics in body environment*, Ishiyaku EuroAmerica, Tokyo, Japan, 1989.
57. P. Fratzl, H. S. Gupta, E. P. Paschalis and P. Roschger, *J. Mater. Chem.*, 2004, **14**, 2115-2123.
58. R. De, A. Zemel and S. A. Safran, in *Methods in Cell Biology*, ed. G. V. Shivashankar, Academic Press, 2010, vol. Volume 98, pp. 143-175.
59. D. Ingber, *Ann. Med.*, 2003, **35**, 564-577.
60. X. Trepat, G. Lenormand and J. J. Fredberg, *Soft Matter*, 2008, **4**, 1750-1759.
61. N. Wang, J. D. Tytell and D. E. Ingber, *Nat. Rev. Mol. Cell Biol.*, 2009, **10**, 75-82.
62. Z. Kalajzic, H. Li, L.-P. Wang, X. Jiang, K. Lamothe, D. J. Adams, H. L. Aguila, D. W. Rowe and I. Kalajzic, *Bone*, 2008, **43**, 501-510.
63. J. M. Zaleskas, B. Kinner, T. M. Freyman, I. V. Yannas, L. J. Gibson and M. Spector, *Biomaterials*, 2004, **25**, 1299-1308.
64. M. Spector, *Wound Repair Regen.*, 2001, **9**, 11-18.
65. B. Kinner, D. M. Pacicca, L. C. Gerstenfeld, C. A. Lee, T. A. Einhorn and M. Spector, *J. Orthop. Res.*, 2003, **21**, 20-27.
66. Y. Liu, B. Deng, Y. Zhao, S. Xie and R. Nie, *Dev., Growth Differ.*, 2013, **55**, 591-605.